The increase of curvature radius of geomagnetic field lines preceding a classical dipolarization

Osuke Saka
Office Geophysik, Ogoori, 838-0141, Japan

Abstract

Based on assumptions that substorm field line dipolarization at geosynchronous altitudes is associated with the arrival of high velocity magnetotail flow bursts referred to as Bursty Bulk Flows, we propose following sequence of field line dipolarization: (1) Slow magnetoacoustic wave excited through Ballooning instability by enhanced inflows in pre-onset intervals towards the equatorial plane; (2) In the equatorial plane, slow magnetoacoustic wave stretching of the flux tube in dawn-dusk directions resulting in spreading plasmas in dawn-dusk directions and reduction in the radial pressure gradient in the flux tube. As a consequence of the foregoing processes, the flux tube assumes a new equilibrium geometry in which curvature radius of new field lines increased in the meridian plane suggesting an onset of field line dipolarization. The dipolarization processes associated with changing the curvature radius preceded classical dipolarization caused by reduction of cross-tail currents and pileup of the magnetic fields.

Increasing curvature radius induced convection surge in the equatorial plane as well as inductive westward electric fields of the order of mV/m. Electric fields transmitted to the ionosphere produce electromotive force in the E layer for generating field-aligned current system of Bostrom type. This is also equivalent to the creation of an incomplete Cowling channel in the ionospheric E layer by the convection surge.

1. Introduction

Substorms are spatially localized and temporarily variable processes in the nighttime magnetosphere. It is often difficult to determine onset timing of substorm processes such as magnetotail flow burst, field line dipolarization, and particle injections. To resolve the timing uncertainties, auroras in global satellite images [Nakamura et al., 2001; Miyashita et al., 2009], intensifications of auroral kilometric radiation [Fairfield et al., 1999; Morioka et al., 2010], and dispersionless particle injection in geosynchronous orbit [Birn et al., 1997] were used. Ground Pi2 pulsations are another useful tool for determination of the substorm timing

[Sakurai and Saito, 1976; Nagai et al., 1998; Baumjohann et al., 1999]. Particularly, Pi2s in equatorial region exhibited small phase difference (m<1, m denotes azimuthal wave number) across widely separated stations in the equatorial countries [Kitamura et al., 1988], minimizing the timing uncertainties arising from delays in longitudinal propagations. This enabled us accurate onset timing study of substorms using magnetometer data from two remote locations, geosynchronous altitudes and ground stations of the equatorial countries [Saka et al., 2010].

In this study, we focus on the dipolarization events at geosynchronous orbit from growth to expansion phase. Triggering mechanisms of the field line dipolarization in the vicinity of geosynchronous orbit are our major concern. In this paper, onset timing study of substorms using magnetometer data from equatorial countries are summarized in Sect. 2. In Sect. 3, we present a pre-onset scenario leading to the dipolarization onset. In Sec.4, excitation of slow magnetoacoustic wave is discussed for triggering field line depolarization. We will focus on the field line dipolarization in the vicinity of geosynchronous orbit in Sect. 5. A coupling of magnetosphere and ionosphere associated with this dipolarization scenario will be presented in Sect. 6. In Sect. 7, we present a triggering mechanism of low latitude Pi2s that enabled the Pi2-based epoch analyses. Summary and discussion of this scenario is given in Sect. 8.

2. Summary of onset timing study using ground Pi2s at the equator

In this section, we summarize field line dipolarization occurring at the geosynchronous orbit based on the statistical results obtained by Saka et al. [2010]. The authors used magnetometer data from geosynchronous satellites (Goes5 and Goes6) and those at ground equatorial stations (Huancayo, Peru, $1.4^{\circ}N$ in geomagnetic latitudes) in the conjugate meridian. Goes5 was located at higher latitudes, $10.3^{\circ}N$ in dipole coordinates, and Goes6 was closer to the equator; $7.9^{\circ}N$ in dipole coordinates. This difference was caused by the separated meridians of the satellites (2.2 hours of local time). The dipole coordinate used are equivalent to the HDV coordinates; H is positive northward along the dipole axis, V is radial outward, and D denotes dipole east. The field line dipolarization at the geosynchronous orbit can be characterized either by a step-like or impulsive increase of inclination angle of the geomagnetic field lines. The inclination angle is measured positive northward from the dipole equator. The step-like dipolarization was observed by Goes5 located at higher latitudes, while the dipolarization pulse was observed by Goes6 at latitudes closer to the equatorial plane.

The onset of field line dipolarization preceded the initial peak of the ground Pi2 pulse by two minutes, suggesting that the onset was initiated in association with the first increase of the Pi2 amplitudes. Following the dipolarization onset, field line magnitude decreased at the

geosynchronous orbit, and field lines deflected westward in the dawn sector and eastward in the dusk sector (see Figure 1 for dawn-dusk deflection, reproduced from [Saka et al., 2010]). This is caused by the dawn-dusk expansion of the plasma flows occurring tailward of the geosynchronous orbit. These longitudinal expansions lasted for about 10 min and decreased the field magnitudes therein. Expansion in the dusk sector, however, continued over this characteristic 10-min-interval. Asymmetries of the dawn-dusk expansion may be caused by diamagnetic drifts in the plasma sheet [Liu et al., 2013]. It is suggested that classical dipolarization, caused by the reduction of cross-tail currents in the midnight magnetosphere, happened after the nightside magnetosphere experienced this characteristic 10-min-interval. For this reason, the first 10 min intervals are referred to as transitional state of substorm expansion [Saka et al., 2010].

3. Pre-onset intervals leading to field line dipolarization

In the pre-onset intervals, decrease of the field line inclination started two hours prior to the dipolarization onset. It attained minimum angles (33.6° for Goes5 and 49.4° for Goes6 in dipole coordinates) right before the dipolarization onset [Saka, 2010; 2019].

One of the properties of plasmas in pre-onset intervals are continuing inflows of lobe plasmas towards the equatorial plane [Birn and Hesse, 1996], Poynting flux enhancement [Machida et al., 2009], and Ey (westward electric fields) penetration toward the equatorial plane [Machida et al, 2014]. Corresponding plasma properties at geosynchronous altitudes may be predominant perpendicular temperature anisotropies of thermal plasmas (30eV - 40keV) obtained from three-dimensional temperature matrix and their gradual decrease towards the onset [Birn et al., 1997]. At the onset, however, increase of parallel anisotropy stopped and perpendicular anisotropy increased again. Such changes of temperature anisotropy at onset were observed in roll-angle spectrogram of energy flux of electrons in 15eV-40keV [Saka and Hayashi, 2017]. This transition of the temperature anisotropies may be accounted for by the following scenario.

A continuing tailward stretch of the field lines in the pre-onset intervals as depicted in Figure 2 may increase equatorward flux by the counterclockwise rotation of the inflow vectors ($F_\perp$) in the north of the equatorial plane (clockwise rotation in the south) and produce a parallel component as well by the relation,

$$\delta F_{//} = F_\perp(\omega \cdot \delta t) \qquad (1)$$

Here, $\delta F_{//}$ denotes increase of parallel flux per time, δt, ω is angular velocity of rotation of $F_{\perp}$ vectors associated with the thinning of the flux tubes caused by stretching. In pre-onset intervals lasting 90 min at geosynchronous altitudes, field line stretching decreased the field line inclination by 7° from 40.6° to 33.6° [Saka, 2019]. This gives angular velocity of rotation of field line inclination in equation (1) as $1.4\times10^{-3}\ rad/\min$. Total parallel flux gained in T min may be given by the integral of equation (1) with time from 0 to T. Substituting T=60 min and $1.4\times10^{-3}\ rad/\min$ for angular velocity of field line inclination, this yields $F_{//}=8.2\times10^{-2}\cdot F_{\perp}$. Gain of $F_{//}$ is about 10% of the perpendicular flux ($F_{\perp}$). This is consistent with the parallel temperature anisotropies gained prior to the onset (20% gain) in geosynchronous orbit [Birn et al., 1997].

Continuing parallel flux flows associated with the flux tube stretching in the pre-onset intervals may increase plasma pressures in the flux tube at its tailward end. This condition leads to further stretching of the flux tube (small curvature radius) [Ohtani and Tamao, 1993; Rubtsov et al., 2018] by the relation,

$$\frac{\beta}{2}\kappa+\kappa_B+\frac{1}{R}=0 \qquad (2)$$

Here, β is plasma to magnetic pressure ratio, κ and κ_B denote reciprocal spatial scales of radial inhomogeneity of plasma pressure and magnetic fields in the equatorial plane, respectively. R is curvature radius of the field lines.

4. Excitation of slow magnetoacoustic wave

The continuing parallel flows may excite magnetoacoustic wave. From a set of linearized MHD equations we have relation between parallel displacement along the field lines (ξ_z) and divergence of perpendicular displacements ($\xi_{\perp}$) in the following form (see Appendix),

$$\xi_z=\frac{C_S^2}{\omega^2}F\cdot B_0^2\frac{\partial}{\partial z}(div\xi_{\perp}) \qquad (3)$$

Here, C_s, ω and B_0 are the sound velocity, angular frequency of waves and background field magnitudes, respectively. F is given by

$$F = \frac{C_A^2}{B_0^2} \frac{1}{C_s^2 - (\frac{\omega}{k})^2} \qquad (4)$$

F is positive for the slow magnetoacoustic wave and negative for the fast magnetoacoustic wave. C_A and *k* denote Alfven velocity and wave vector, respectively. We use equation (3) for the classification of slow and fast magnetoacoustic waves. Slow magnetoacoustic wave yields perpendicular expansion of the flux tubes at the converging point of parallel flows on the equatorial plane. For fast wave, perpendicular shrinkage of flux tubes occurs at the converging point of parallel flows (equatorial plane).

The equation (3) will be applied to simulate possible effect of magnetoacoustic wave on pitch angle spectrogram. For this, we used drift Maxwell distributions for phase space density (PSD) assuming gyrotropy for particle trajectories. PSD was composed of three parts: one drifting parallel, another anti-parallel along the field lines, and the third part perpendicular to the field lines. Figure 3(A) shows pitch angle spectrogram of energy flux with no drift velocities either perpendicular or parallel to the background field lines. Energy flux is defined by $\left(2E^2/m^2\right) f$, where *E*, *m*, *f* are energy, mass of particles, and phase space density, respectively. Energy flux is given in $eV/(cm^2 s \cdot sr \cdot eV)$. Only parallel drift increased in from $0.3V_{th}$, $0.6V_{th}$, and to $1.0V_{th}$ as shown in B, C, and D. For E and F, perpendicular drift increased to $0.3V_{th}$ and $0.5V_{th}$ while parallel drift remained at $1.0V_{th}$. Energy fluxes initially in quasi trapped distribution (A) changed to more parallel and anti-parallel fluxes as parallel and anti-parallel drift increased (B, C, and D). Increasing perpendicular drifts increased perpendicular fluxes in the pitch angle distributions of E and F.

We clarified that magnetoacoustic wave produced coupling of parallel flux along the field lines and the perpendicular flux. However, we choose slow magnetoacoustic wave for the wave mode because the flux tubes expanded (did not shrink) in the transitional interval as discussed in Section 2. Slow magnetoacoustic wave may be triggered through Ballooning instability, when enough pressure gradient is accomplished in an earthward direction [Ohtani and Tamao,1989; Rubtsov et al., 2018].

We can estimate the Ballooning instability threshold κ (reciprocal scale of radial inhomogeneity of plasma pressure) using calculation results given in [Rubtsov et al., 2018]. In a distance from L=5 to 10Re, instability threshold is given approximately as $\kappa = -1.0\,\mathrm{Re}^{-1}$ (κ denotes reciprocal spatial scale of radial inhomogeneity of plasma pressure, and Re is the Earth radius) for beta defined by the ratio of plasma pressure and magnetic pressure exceeding 0.1. This suggests that the Ballooning instability develops at the geosynchronous altitudes (curvature radius R is 2.2 Re) when spatial scale of the earthward pressure gradient

caused by the inflows becomes steeper than 1.0 Re. We show in the following section that this theoretical consideration matched observations.

5. Field line dipolarization in the vicinity of geosynchronous orbit

5.1 Relaxation of radial inhomogeneity

We can assume the westward electric fields in Dipolarization Front (DF) [Runov et a., 2011] embedded in the leading edge of Bursty Bulk Flow (BBF) as external stimulus for triggering Ballooning instability. In this case westward electric fields in the DF temporarily amplified the parallel flux flowing towards the end point of the flux tube in the equatorial plane and further steepen earthward pressure gradient. If it exceeds instability threshold determined by β and initial curvature radius *R*, slow magnetoacoustic wave can be excited [Rubtsov et al., 2018]. Once the slow magnetoacoustic wave was excited, perpendicular fluxes spread the plasmas in dawn-dusk directions and smooth (or relax) the radial gradient of plasma pressures in the equatorial plane (smaller κ). This may result in the transition of the flux tube geometry to a new configuration, an increase of the curvature radius of the field lines (larger *R*) (see equation (2)).

We revisit multiple Pi2 events observed by AMPTE CCE on 31 August 1986 [Saka et al., 2002] and show an example of relaxation of radial inhomogeneity of plasma pressures associated with field line dipolarization in Figure 4. The satellite passed the midnight sector (20 – 23 MLT) from 3 Re to 7 Re at latitudes south of the equatorial plane (-8° MLat) when multiple Pi2 event (with positive bay) were observed at low latitude station (KUJ) at L=1.2 in the midnight sector (Figure 4A). Inclination angle of field lines along the satellite trajectory is shown in Figure 4(B). Dipolarization occurred as marked by vertical arrows correlating to multiple onset of Pi2s, 1 through 4 in Figure 4(A). Ion fluxes coming from dawn sector ($\mathbf{J}_-$) and from dusk sector ($\mathbf{J}_+$) at satellite altitudes were measured by the instruments (two energy channels, 63-85 keV and 125-210 keV) on board AMPTE CCE [Takahashi et al., 1996]. A schematic of particle measurement is shown at the top of Figure 5. The flux difference ($\mathbf{J}_- - \mathbf{J}_+ > 0$) increased in association with the onset of multiple Pi2 (15:05 UT) and positive bay at KUJ (Figures 4C and 4D). Sudden increase was followed by the slow decrease of flux in 63-85 keV channel and rapid decrease of flux in 125-210 keV channel. The flux difference, $\mathbf{J}_- > \mathbf{J}_+$, may be caused either by earthward pressure gradient or

198 westward convection of plasmas. From the different patterns of the flux decrease with time
199 in two energy channels, we can suggest that the measured flux difference, $\mathbf{J}_- - \mathbf{J}_+$, can be
200 attributed to increase of the earthward pressure gradient and succeeding relaxation. Note
201 that guiding center of $\mathbf{J}_- / \mathbf{J}_+$ is earthward/tailward of the satellite position as depicted in
202 top of Figure 5. The different relaxation speed in two energy channels, slower for 63-85 keV
203 and faster for 125-210 keV, suggest that the earthward pressure gradient (assumed to be
204 proportional to the flux gradient) decreased with time during the multiple Pi2 event (Figure 5).
205 The flux difference (50 counts/sample) was 10% of the background flux both for 63-85 keV
206 (Larmor radius is 250 km for 150 nT) and for 125-210 keV (Larmor radius is 450 km), that is,
207 the flux level differed by 10% at two locations 1000 km apart in radial distance for 63-85 keV
208 and 1800 km for 125-210 keV. This gives e-folding scale of the earthward pressure gradient
209 being 0.98 Re and 1.77 Re for 63-85 keV and 125-210 keV, respectively. The 31 August
210 event shows that radial pressure gradient was relaxed in the inner magnetosphere in
211 association with the increase of the field line inclination (dipolarization). Although the field line
212 dipolarization showed a sharp onset in satellite magnetometer data, we note that it did not
213 occur in ion flux data. This may be true because the ion flux change at the onset may be
214 obscured by the contamination from the past onsets transported across the field lines from
215 the adjoining sector by the electric fields and gradient/curvature drifts. We conclude that the
216 relaxation of spatial inhomogeneity started when the spatial scale of the radial inhomogeneity
217 approached 1.0 Re, consistent with theoretical consideration of Ballooning instability by
218 Rubtsov et al (2018).
219
220 *5.2 Flux tube transition to a new geometry*
221 Meanwhile, field lines in the further earthward locations may be compressed by the inward
222 movement of the outer field lines. This process associated with the dipolarization onset may
223 increase the parameter κ_B in equation (2) which may result in transition to a new geometry
224 of earthward field lines, a decrease of the curvature radius *R*. Transition of the field line
225 geometries for onset locations and ones in earthward locations are schematically illustrated
226 in Figure 6. These field line geometries in meridian plane matched the third harmonic and
227 fundamental harmonic deformations of outer and inner field lines, respectively. This is often
228 observed in the midnight magnetosphere in the initial pulse of Pi2s [Saka et al., 2012].
229 Transitions of the flux tube geometry in magnetosphere also correspond to the production of
230 negative bay in higher latitudes and positive bay in lower latitudes. If we can assume that
231 negative bay switched to positive bay at latitudes, 60 degrees in geomagnetic coordinates

for examples, this latitude can be mapped beyond the geosynchronous orbit (L~7 Re or further tailward) as field line dipolarization occurs along the stretched flux tubes. Consequently, this scenario requires that the BBFs are not necessary to reach inner magnetosphere to trigger the substorm onset at lower latitudes. In the inset, flux tube deformations are illustrated in the equatorial cross section at onset locations (field lines 1 and 2). Divergence of perpendicular flows (solid arrows) produced dawn-dusk expansion of flux tube (2) and the shrinkage of stretched flux tube (1) by relaxation of the radial inhomogeneity. Flux tube deformation from 1 to 2 tended to preserve the total magnetic fluxes in the equatorial cross section. From the local time distribution of the dawn-dusk expansion of the flux tubes shown in Figure 1, most of the flux tube transition such as from 1 to 2 may occur tailward of geosynchronous orbit. Some of the events, however, may happen earthward of the geosynchronous orbit [i.e., Ohtani et al., 2018].

Increasing of the curvature radius, or earthward shrinkage of the flux tubes, produce a reduction of the radial component of the field lines (V in dipole coordinates) by adding positive V in the north of the equatorial plane and negative V in the south. If amplitudes of the V component changed by 10 nT in one minute, the expected inductive electric fields (westward) could be of the order of 1.0 mV/m when shrinkage was confined within 1 Re from the equatorial plane. The dawn-dusk expansion of the flux tubes may also produce inductive electric fields (earthward and tailward in dawn and dusk sector, respectively) of the same order of magnitudes. They are Alfven waves, a wave mode in Ballooning instability coupled with slow magnetoacoustic wave [Rubtsov et al., 2018]. The westward electric fields produce earthward flow bursts referred to as convection surge. The inductive electric fields produced by the dipolarization are the same order of magnitudes observed in DF [Runov et al., 2011].

6. Coupling of magnetosphere and ionosphere in association with field line dipolarization

The inductive electric fields may be transmitted along the field lines as poloidally and toroidally polarized Alfven waves [Klimushkin et al., 2004]. These electric fields produce a dynamic ionosphere in polar region that includes nonlinear evolution of ionospheric plasmas (poleward expansion), as well as production of field-aligned currents and parallel potentials by exciting ion acoustic wave in quasi-neutral condition [Saka, 2019]. It is not the aim of this paper to describe in detail the dynamic processes in the ionosphere, but to show a local production of currents in the ionosphere as well as field-aligned currents by the penetrated electric fields. For this purpose, we revisit the 10 August 1994 substorm event studied by Saka and Hayashi (2017). In this event, eastward expansion was observed of the field line dipolarization region, started at 11:55 UT (00:27 MLT) from 260° E of geomagnetic longitudes

and expanded to 351° E in about 48 min. At the leading edge of the expansion, ground magnetometer data showed bipolar event (quick change of the D component from positive to negative in about 5 min), being confined in the expanding dipolarization front as a substructure. The substructure in the leading edge of the field line dipolarization will be examined as follows.

We can assume that magnetic signals on the ground are associated with the sum of the horizontal Hall currents in the ionosphere [Fukushima, 1971]. These currents can be calculated by the relation,

$$(rot\,\mathbf{J})_Z = -\frac{1}{\mu_0}\nabla^2 B_Z \qquad (5)$$

We used the ground vertical component (b) as a proxy of B_z in the ionosphere. The second derivative in right-hand side of equation (5) is approximated as,

$$\nabla^2 B_Z^i = \left(\frac{b^{i+1}-b^i}{L_{i+1}-L_i} - \frac{b^i - b^{i-1}}{L_i - L_{i-1}}\right) / (L_{i+1} - L_{i-1}) \qquad (6)$$

Here, i denotes i-th station in the meridian chain. L_i is the geomagnetic latitude of the i-th station. We considered meridional change only. This is because the vertical component changed from negative to positive across the meridian, while in longitudes it changed simply decreasing or increasing in lower and higher latitudes after onset, respectively. Hence, longitudinal variations may contribute less to the Laplacian. The results reproduced from Saka and Hayashi (2017) are shown in Figure 7(A). The eastward propagation of dipolarization front crossed this meridian (300° E) at 12:13 UT corresponding to the interval labelled 1. Two points arose from this figure; (1) Loop of Hall current pair existed, CCW viewed from above the ionosphere in the lower latitudes and CW in the higher latitudes, (2) These current patterns expand poleward. Current patterns in the interval from 1 to 5 in Figure 7(A) are illustrated in Figure 7(B) to facilitate the poleward expansion. It is clearly demonstrated that current pair forming CW in higher latitudes and CCW in lower latitudes expanded in time towards the pole. Bipolar change can be recorded in the D component data (not shown) when the ground station, FSIM in this case, passes from segment 1 to 2 in Figure 7(B). As a result, dipolarization front expanded eastward progressively by producing the poleward expansion at each meridian. The front left behind the current pattern comprising upward field-aligned currents in lower latitudes and downward in higher latitudes, or Bostrom type current system. We propose that the ionosphere itself has inherent electromotive force to drive this Bostrom type current system. The reasons are as follows.

In the E region, drift trajectories may be written [Kelley, 1989] for electrons by,

$$\mathbf{U}_{e\perp} = \frac{1}{B}[\mathbf{E}\times\hat{\mathbf{B}}] \qquad (7)$$

and for ions by,

$$\mathbf{U}_{i\perp} = b_i[\mathbf{E} + \kappa_i\mathbf{E}\times\hat{\mathbf{B}}]. \qquad (8)$$

Here, b_i is mobility of ions defined as $\Omega_i/(B\nu_{in})$, κ_i is defined as Ω_i/ν_{in}. Symbols Ω_i and ν_{in} are ion gyrofrequency and ion-neutral collision frequency, respectively. $\hat{\mathbf{B}}$ denotes a unit vector of the magnetic fields B. We assumed that $\mathbf{E}\times\mathbf{B}$ drifts for electrons and ions were driven by westward electric fields transmitted from the convection surge. Because of very low mobility of ions in E layer ($\kappa_i = 0.1$), electric field drifts accumulate electrons (not ions) in lower latitudes and produce stronger secondary southward electric fields in the ionosphere. The southward electric fields produced southward motion of ions due to the first term of equation (8). They carry Pedersen currents (ion currents) for producing quasi-neutrality of ionosphere. $\mathbf{E}_W\times\mathbf{B}$ drifts caused by the transmitted westward electric fields ($\mathbf{E}_W$) may propel electrons against southward electric fields from higher latitudes to lower latitudes as electromotive force to maintain the potential drop for driving Pedersen currents. This means the ionospheric E layer contains both generator and load in it. In quasi-neutral condition, a small imbalance of particle densities of electrons and ions ($n_e - n_i \sim 10^2 m^{-3}$) may induce in lower latitudes negative potential region of the order of -100 kV with horizontal scale length of 100 km. To sustain this negative potential, upward field-aligned currents of the order of $1.0\mu A/m^2$ for $\Sigma_P \sim 10^0 S$ must flow. Downward field-aligned currents from the positive potential regions in the higher latitudes may also be expected. It is supposed that upward field-aligned currents may be carried mostly by ions flowing outwards and downward currents are escaping electrons to the magnetosphere. Those ions and electrons escape from the ionosphere into the magnetosphere to assure quasi-neutral conditions of the ionosphere. The above scenario may be adapted to a creation of the incomplete Cowling channel [Baumjohann, 1983], where unbalanced primary northward Hall currents and secondary southward Pedersen currents driven by the polarization electric fields yielded field-aligned currents.

7. Triggering mechanisms of low latitude Pi2s

From ground magnetometer observations in auroral zone, it is natural to assume that flux tubes linked to negative bay (decreasing of the H component) and positive bay (increasing of the H component) at higher and lower latitudes, respectively, oscillated coherently at Pi2 periods. Oscillating flux tubes associated with positive bay may produce local compression of magnetic fields in the equator and trigger cavity mode in low latitudes [Takahashi et al., 1995]. Oscillations, however, are short-lived and may not establish true cavity modes. They excite cavity/waveguide modes in the plasmasphere [Allan et al., 1996; Li et al., 1998].

In the dip-equator, a singular latitude of the cavity/waveguide mode, only isotropic mode can be excited [Allan et al., 1996]. This leads us to suppose that a very large propagation velocity (or large wavelength exceeding whole circle of the Earth) of equatorial Pi2s in the nightside sector [Kitamura et al., 1988] would be associated with the dawn-dusk asymmetries of non-propagating compressions.

Pi2 periodicity may be determined primary by consecutive arrival of BBF substructures referred to as dipolarization front bundle (DFB) [Liu et al., 2013, 2014]. Repeating arrival of DFB produces periodic dipolarization or oscillation of negative bays. Positive bay oscillations in the plasmasphere would follow the negative bay oscillations to excite cavity/waveguide modes for low to equatorial Pi2s at the same periodicities. To estimate the onset time of the field line dipolarization using the very low latitudes Pi2s, delays in transmission are from the magnetosphere; longitudinal delays across the meridian may not be significant.

High latitude Pi2s may not be caused by cavity/waveguide modes but by oscillation of field-aligned currents comprising Bostrom type current system (incomplete Cowling channel), R1 (region 1) type current system associated with convection surge [i.e., Birn and Hesse, 1996], and R2 (region 2) type current system of expanding flux tubes in longitudes [i.e., Tanaka et al., 2010]. In contrast to the very-low latitude Pi2s associated with the non-propagating compression, the high-latitude Pi2s propagated on the ground typically at 20km/s eastward and westward in the sector east and west of the substorm center, respectively [Samson and Harrold, 1985]. Propagation across the meridian may cause further delays, 35 sec for propagation of 1 hour of local time. We should exercise caution when using high latitude Pi2s for timing study.

The above scenario assumes that the DFBs arrived periodically in the inner magnetosphere at a frequency not very different than the cavity frequency of plasmasphere.

8. Discussion and Summary

Definition of field line dipolarization is a configuration change from stretching to shrinkage of geomagnetic field lines in the midnight meridian of magnetosphere. Two models have been proposed to account for the configuration change; diversion of the cross-tail currents via ionosphere, referred to as substorm current wedge (SCW), as first proposed in McPherron et al. [1973] and extinction of the cross-tail currents by a local kinetic instability, current disruption (CD) [Lui, 1996]. These models have been adopted for many decades to account for the critical issues associated with substorm onset. We propose, based on Ballooning instability scenario, that field line dipolarization is caused by the relaxation of radial inhomogeneity of plasma pressures in association with the excitation of slow magnetoacoustic wave. Dipolarization regions expand in longitudes and decrease field magnitudes by expanding flux tubes therein. This condition continued for about 10 min and classical dipolarization caused by the reduction of cross-tail currents or pileup of the magnetic flux transported from the tail begins.

It is noted that BBFs with low entropy plasmas (plasma bubbles) often penetrated to the inner magnetosphere [Dubyagin et al., 2011]. In numerical simulations, those bubbles localized in local time produced global dipolarization in the inner magnetosphere [Merkin et al., 2019] and generated ionospheric current system such as westward electrojet, Harang discontinuity, and poleward expansion of aurora in substorm expansion phase [Yang et al., 2012]. These classical features of substorm expansion occurred in this first 10 min intervals of Pi2 onset referred to as transitional intervals in the midnight magnetosphere. The transitional intervals may be the most active periods in the substorm phase.

The proposed scenario was deduced from the geosynchronous observation and cannot be readily applied to the onset scenario beyond the geosynchronous orbit. Nevertheless, dawn-dusk expansion of the flux tubes may be a fundamental property of field line dipolarization not only at geosynchronous altitudes but also in tailward locations (8 - 12 Re) [Yao et al., 3013; Liu et al., 2013]. It is suggested that the field line dipolarization at tailward locations is subdivided by faster expanding (in longitudes) dipolarization front (DF) and slower expanding dipolarization front bundle (DFB) led by DF [Liu et al., 2015]. Such substructures in field line dipolarization are also observed at geosynchronous altitudes [Saka and Hayashi, 2017]. The geosynchronous dipolarization expanded (in longitudes) at 1.9 km/s, while Pi2s emitted in the dipolarization region propagated one order of magnitude faster. The fast longitudinal velocities associated with Pi2s may be embedded within the slowly expanding region of dipolarization, similarly to the relationship between DF and DFB. If this relationship can be adapted also to the transitional state and succeeding field line pileup, the dipolarization scenario at geosynchronous observations can be extended further tailward in upstream. Or,

the onset scenario in 10 Re can be applied in geosynchronous dipolarization. In that case, dipolarization pulse at Goes6 latitudes ($7.9^{\circ} N$) may represents DFs. This assumption may be supported because electron energy flux pitch angle distributions in tailward locations beyond 10Re show parallel to perpendicular transitions, like ones in Figure 3, at the arrival of DF [Deng et al., 2010].

We emphasize that two different types of the dipolarization exist in the substorms; one is associated with change of curvature radius of field lines in the transitional state (faster expansion in longitudes) and the other is subsequent pileup of the magnetic flux transported from the tail (slower expansion). Field line pileup caused by the flow braking processes [Shiokawa et al., 1997] may lead to tailward regression of the dipolarization region as reported in Baumjohann et al. [1999].

In the transitional state lasting for about 10 min, the inductive electric fields pointing westward were produced in the equatorial plane. They propagated along the field lines to the ionosphere to produce meridional field-aligned currents of the Bostrom type (downward in higher latitudes and upward in lower latitudes). The Bostrom type current system was indeed observed on the ground at the front of dipolarization expanding towards east. The magnetospheric dynamo produced by earthward electric fields in the equatorial plane [Akasofu, 2003] and the E layer dynamo in the ionosphere worked together to activate the Bostrom current system.

9. Code/Data availability

Satellite data from Goes5/6, AMPTE CCE and ground magnetometer data in Figures 1, 4 and 7 is available upon request to Osuke Saka (saka.o@nifty.com).

10. Competing interest

The author declares that there is no conflict of interest.

Acknowledgements

The author would like to express his sincere thanks to all the members of Global Aurora Dynamics Campaign (GADC) [Oguti et al., 1988]. We are also grateful to anonymous referees for their critical review.

Appendix

435 In order to derive equations (3) and (4), we first follow Kadomtsev (1979). Linearized MHD
436 equations may be written as,

437 $$\frac{\partial^2 \boldsymbol{\xi}}{\partial t^2} = C_S^2 \nabla div\boldsymbol{\xi} + C_A^2 \nabla_\perp div\boldsymbol{\xi}_\perp + C_A^2 \frac{\partial^2 \boldsymbol{\xi}_\perp}{\partial z^2}. \qquad \text{(A1)}$$

438 Here, C_S, C_A, $\boldsymbol{\xi}$ denote sound velocity, Alfven velocity, plasma displacement, respectively.
439 $(\perp, z)$ denote perpendicular and parallel component with respect to the background field
440 lines.
441 After a few manipulations of (A1), we have magnetoacoustic wave equations for finite β
442 plasmas:

443 $$\frac{\partial^2 div\boldsymbol{\xi}_\perp}{\partial t^2} = C_A^2 \Delta div\boldsymbol{\xi}_\perp + C_S^2 \Delta_\perp div\boldsymbol{\xi} \qquad \text{(A2)}$$

444 and

445 $$\frac{\partial^2 \xi_z}{\partial t^2} = C_S^2 \frac{\partial}{\partial z}\left(div\boldsymbol{\xi}\right) \qquad \text{(A3)}$$

446 Equations (A2) and (A3) present compressive properties across and along the background
447 field lines, respectively.
448 Assuming plane harmonic wave solutions, first order quantities of density and magnetic field
449 compressions $(\delta n, \delta \mathbf{B})$ may be given by the following equation.

450 $$\frac{\delta n}{n_0} = -\frac{C_A^2}{B_0^2} \frac{1}{C_S^2 - \left(\frac{\omega}{k}\right)^2} \left(\mathbf{B}_0 \cdot \delta \mathbf{B}\right) \qquad \text{(A4)}$$

451 Here, n_0, B_0 denote background density and magnetic fields, respectively.

452 Substitution of (A4) into (A3) using $div\boldsymbol{\xi} = -\delta n / n_0$ yields

453 $$\frac{\partial^2 \xi_z}{\partial t^2} = C_S^2 F \frac{\partial}{\partial z}\left(\mathbf{B}_0 \cdot \delta \mathbf{B}\right). \qquad \text{(A5)}$$

454 Here, $F = \frac{C_A^2}{B_0^2} \frac{1}{C_S^2 - \left(\frac{\omega}{k}\right)^2}$

455 Linearized Faraday's law in frozen-in condition, $\delta \mathbf{B} = \nabla \times (\boldsymbol{\xi}_\perp \times \mathbf{B}_0)$, may be reduced to

456 $$\delta \mathbf{B} = -\mathbf{B_0} div\boldsymbol{\xi}_\perp + B_0 \frac{\partial}{\partial z} \boldsymbol{\xi}_\perp. \qquad \text{(A6)}$$

457 Substituting (A6) into (A5), we have final expressions relating parallel and perpendicular
458 displacements as,

$$\frac{\partial^2 \xi_z}{\partial t^2} = -C_S^2 F \cdot B_0^2 \frac{\partial}{\partial z}\left(div \boldsymbol{\xi}_\perp\right). \quad \text{(A6)}$$

Replacing $\partial/\partial t$ with $-i\omega$, (A6) yields the equation (3) in Section 4,

$$\xi_z = \frac{C_S^2}{\omega^2} F \cdot B_0^2 \frac{\partial}{\partial z}(div \xi_\perp).$$

References

Akasofu, S.-I.: Source of auroral electrons and the magnetospheric substorm current system, J. Geophys. Res., 108, A4, 8006, doi:10.1029/2002JA009547, 2003.

Allan, W., F.W. Menk, B.J. Fraser, Y. Li, and S.P. White, Are low-latitude Pi2 pulsations cavity/waveguide mode?, Geophys. Res. Lett., 23, 765, 1996.

Baumjohann, W.: Ionospheric and field-aligned current systems in the auroral zone: A concise review, Adv. Space Res., 2, 55-62, 1983.

Baumjohann, W., Hesse, M., Kokubun, S., Mukai, T., Nagai, T., and Petrukovich, A.A.: Substorm dipolarization and recovery, J. Geophys. Res., 104, 24995-25000, 1999.

Birn, J., and Hesse, M.: Details of current disruption and diversion in simulations of magnetotail dynamics, J.Geophys.Res., 101, A7, 15345-15358, 1996.

Birn, J., Thomsen, M.F., Borovsky, J.E., Reeves, G.D., McComas, D.J., and Belian, R.D.: Characteristic plasma properties during dispersionless substorm injections at geosynchronous orbit, J. Geophys. Res., 102, A2, 2309-2324, 1997.

Deng, X, Ashour-Abdalla, M., Zhou, M., Walker, R., El-Alaoui, M., Angelopoulos, V., Ergun, R.E., and Schriver, D.: Wave and particle characteristics of earthward electron injections associated with dipolarization fronts, J.Geophys.Res., 115, A09225, doi:10.1029/2009JA015107, 2010.

Dubyagin, S., Sergeev, V., Apatenkov, S., Angelopoulos, V., Runov, A., Nakamura, R., Baumjohann, W., McFadden, J., and Larson, D.: Can flow bursts penetrate into the inner magnetosphere?, Geophys.Res.Lett., 38, L08102, doi:10.1029/2011GL047016, 2011.

Fairfield, D.H., Mukai, T., Brittnacher, M., Reeves, G.D., Kokubun, S., Parks, G.K., Nagai, T., Mtsumoto, H., Hashimoto, K., Gurnett, D.A., and Yamamoto, T.: Earthward flow bursts in the inner magnetotail and their relation to auroral brightenings, AKR intensifications, geosynchronous particle injections and magnetic activity, J. Geophys. Res., 104, A1, 355-370, 1999.

492 Fukushima, N.: Electric current systems for polar substorms and their magnetic effect below
493 and above the ionosphere, Radio Sciences, 6, 269-275, 1971.
494 Kadomtsev, B.B.: Collective phenomena in plasmas (in Japanese), Iwanami shoten, Tokyo,
495 1979. (English edition published in 1982 is available from Pergamon Press)
496 Kelley, M.C.: The earth's ionosphere: plasma physics and electrodynamics, Academic Press,
497 Inc, 1989.
498 Kitamura, T., Saka, O., Shimoizumu, M., Tachihara, H., Oguti, T., Araki, T., Sato, N., Ishitsuka,
499 M., Veliz, O., and Nyobe, J.B.: Global mode of Pi2 waves in the equatorial region:
500 Difference of Pi2 mode between high and equatorial latitudes, J. Geomag. Geoelectr,
501 40, 621-634, 1988.
502 Klimushkin, D.Yu., Mager, P.N., and Glassmeier, K.-H.: Toroidal and Poloidal Alfven waves
503 with arbitrary azimuthal wave numbers in a finite pressure plasma in the Earth's
504 magnetosphere, Annales Geophysicae, 22, 267-287, 2004.
505 Li, Y., B.J. Fraser, F.W. Menk, D.J. Webster, and K. Yumoto, Properties and sources of low
506 and very low latitude Pi2 pulsations, J. Geophys. Res., 103, 2343, 1998.
507 Liu, J., Angelopoulos, V., Runov, A., and Zhou, X.-Z.: On the current sheets surrounding
508 dipolarizing flux bundles in the magnetotail: The case for wedgelets, J.Geophys.Res.,
509 118, 2000-20120, doi:10.1002/jgra50092, 2013.
510 Liu, J., Angelopoulos, V., Zhou, X.-Z., and Runov, A.: Magnetic flux transport by dipolarizing
511 flux bundles, J.Geophys.Res., 119, 909-926, doi:10.1002/2013JA019395, 2014.
512 Liu, J., Angelopoulos, V., Zhou, X.-Z., Yao, Z.-H., and Runov, A.: Cross-tail expansion of
513 dipolarizing flux bundles, J.Geophys.Res., 120, 2516-2530,
514 doi:10.1002/2015JA020997, 2015.
515 Lui, A.T.Y.: Current disruption in the Earth's magnetosphere: Observations and models, J.
516 Geophys. Res., 101, 13067-13088, 1996.
517 Machida, S., Miyashita, Y., Ieda, A., Nose, M., Nagata, D., Liou, K., Obara, T., Nishida, A.,
518 Saito, Y., and Mukai, T.: Statistical visualization of the Earth's magnetotail based on
519 Geotail data and the implied substorm model, Ann. Geophys., 27, 1035-1046, 2009.
520 Machida, S., Miyashita, Y., Ieda, A., Nose, M., Angelopoulos, V., and McFadden, J.P.:
521 Statistical visualization of the Earth's magnetotail and the implied mechanism of
522 substorm triggering based on superposed-epoch analysis of THMIS data, Ann.
523 Geophys., 32, 99-111, 2014.
524 McPherron, R.L., Russell, C.T., and Aubry, M.P.: Satellite studies of magnetospheric
525 substorms on August 15, 1968: 9. Phenomenological model for substorms, J.
526 Geophys. Res., 78, 3131-3148, 1973.
527 Merkin, V.G., Panov, E.V., Sorathia, K.A., and Ukhorskiy, A.Y.: Contribution of bursty bulk

528 flows to the global dipolarization of the magnetotail during an isolated substorm,
529 J.Geophys.Res., 124, 8647-8668, https://doi.org/10.1029/2019JA026872.
530 Miyashita, Y., Machida, S., Kamide, Y., Nagata, D., Liou, K., Fujimoto, M., Ieda, A., Saito,
531 M.H., Russell, C.T., Christon, S.P., Nose, M., Frey, H.U., Shinohara, I., Muaki, T., Saito,
532 Y., and Hayakawa, H.: A state-of-the-art picture of substorm-associated evolution of
533 the near-Earth magnetotail obtained from superposed epoch analysis, J. Geophys.
534 Res., 114, A01211, doi:10.1029/2008JA013225, 2009.
535 Morioka, A., Miyoshi, Y., Miyashita, Kasaba, Y., Misawa, H., Tsuchiya, F., Kataoka, R.,
536 Kadokura, A., Mukai, T., Yumoto, K., Menietti, D.J., Parks, G., Liou, K., Honary, and
537 Donovan, E.: Two-step evolution of auroral acceleration at substorm onset, J.
538 Geophys. Res., 115, A11213, doi:10.1029/2010JA015361, 2010.
539 Nagai, T., Fujimoto, M., Saito, Y., Machida, S., Terasawa, T., Nakamura, R., Yamamoto, T.,
540 Mukai, T., Nishida, A., and Kokubun, S.: Structure and dynamics of magnetic
541 reconnection for substorm onsets with Geotail observations, J. Geophys. Res., 103,
542 A3, 4419-4440, 1998.
543 Nakamura, R., Baumjohann, W., Brittnacher, M., Sergeev, V.A., Kubyshkina, Mukai, T., and
544 Liou, K.: Flow bursts and auroral activations: Onset timing and foot point location, J.
545 Geophys. Res., 106, A6, 10777-10789, 2001.
546 Oguti, T., Kitamura, T., and Watanabe, T.: Global aurora dynamics campaign, 1985-1986, J.
547 Geomag. Geoelectr, 40, 485-504, 1988.
548 Ohtani, S.-I., Miura, A., and Tamao, T.: Coupling between Alfven and slow magnetosonic
549 waves in an inhomogeneous finite-β plasma: 1 Coupled equations and physical
550 mechanism, Planet. Space Sci., 37, 567-577, 1989.
551 Ohtani, S.-I., and Tamao, T.: Does the ballooning instability trigger substorms in the near-
552 earth magnetotail?, J. Geophys. Res., 98, A11, 19369-19379, 1993.
553 Ohtani, S.-I., Motoba, T., Gkioulidou, M., Takahashi, K., and Singer, H.J.: Spatial development
554 of the dipolarization region in the inner magnetosphere, J.Geophys.Res., 123, 5452-
555 5463, doi.org/10.1029/2018JA025443.
556 Rubtsov, A.V., Mager, P.N., and Klimushkin, D.Yu.: Ballooning instability of azimuthally small
557 scale coupled Alfven and slow magnetoacoustic modes in two-dimensionally
558 inhomogeneous magnetospheric plasma, Physics of Plasmas 25, 102903,
559 doi:10.1063/1.5051474, 2018.
560 Runov, A., Angelopoulos, V., Zhou, X.-Z., Zhang, X.-J., Li, S., Plaschke, F., and Bonnell, J.:
561 A THEMIS multicase study of dipolarization fronts in the magnetotail plasma sheet,
562 116, A05216, doi:10.1029/2010JA016316, 2011.
563 Saka, O., Akaki, H., and Baker, D.N.: A satellite magnetometer observation of dusk-to-dawn

current in the midnight magnetosphere at low-latitude Pi2 onset, Earth Planets Space, 54, e1-e4, 2002

Saka, O., Hayashi, K, and Thomsen, M.: First 10 min intervals of Pi2 onset at geosynchronous altitudes during the expansion of energetic ion regions in the nighttime sector, J. Atmos. Solar Terr. Phys., 72, 1100-1109, 2010.

Saka, O., Hayashi, K., and Koga, D.: Excitation of the third harmonic mode in meridian planes for Pi2 in the auroral zone, J. Geophys. Res., 117, A12215, doi:10.1029/2012JA018003, 2012.

Saka, O., and Hayashi, K.: Longitudinal expansion of field line dipolarization, J. Atmos. Solar Terr. Phys., 164, 235-242, 2017.

Saka, O.: A new scenario applying traffic flow analogy to poleward expansion of auroras, Ann. Geophys., 37, 381-387, 2019.

Sakurai, T., and Saito, T.: Magnetic pulsation Pi2 and substorm onset, Planet. Space Sci., 24, 573-575, 1972.

Samson, J.C., and B.G. Harrold, Characteristic time constant and velocities of high-latitude Pi2's, J. Geophys. Res., 90, 12173, 1985.

Shiokawa, K., Baumjohann, W., and Haerendel, G.: Braking of high-speed flows in the near-Earth tail, J.Geophys.Res., 24, 10, 1179-1182, 1997.

Takahashi, K., Ohtani, S.-I., and Anderson, B.J.: Statistical analysis of Pi2 pulsations observed by the AMPTE CCE spacecraft in the inner magnetosphere, J.Geophys.Res., 100, A11, 21929-21941, 1995.

Takahashi, K., Anderson, B.J., and Ohtani, S.-I.: Multisatllite study of nightside transient toroidal waves, J.Geophys.Res., 101, A11, 24815-24825, 1996.

Tanaka,T., Nakamizo, A., Yoshikawa, A., Fujita, S., Shinagawa, H., Shimazu, H., Kikuchi, T., and Hashimoto, K.K.: Substorm convection and current system deduced from the global simulation, J.Geophys.Res. 115, A05220, doi:10.1029/2009JA014676, 2010.

Yang, J., Toffoletto, F.R., Wolf, R.A., Sazykin, S., Ontiveros, P.A., and Weygand, J.M.: Large-scale current systems and ground magnetic disturbance during deep substorm injections, J.Geophys.Res., 117, A04223, doi:10.1029/2011JA017415, 2012.

Yao, Z, Sun, W.J., Fu, S.Y., Pu, Z.Y., Liu, J., Angelopoulos, V., Zhang, X.-J., Chu, X.N., Shi, Q.Q., Guo, R.L., and Zong, Q.-G.: Current structures associated with dipolarization fronts, J.Geophys.Res., 118, 6980-6985, doi:10.1002/2013JA019290, 2013.

600 Figure captions
601
602 Figure 1.
603 Upper panel: Local time distribution of W event and E event (see below). Lower panels:
604 Epoch superposition of field line deflections in degrees for Goes5/6. Those events with
605 eastward deflections (clockwise rotation, azimuth angle decreased) at T=0 shown to the left
606 (E event) and those with westward deflections (counterclockwise rotation, azimuth angle
607 increase) at T=0 are to the right (W event). T=0 marked by vertical dotted lines corresponds
608 to the first peak of the Pi2 waveform. Amplitudes at the onset (T=0) were subtracted from the
609 original data to adjust the pre-onset level. Plots covered 40 min from T-10 min to T+30 min.
610 Mean value of the epoch plot and mean value of band-passed (6-20 mHz: Pi2 band)
611 amplitudes are also shown. The field line rotations projected to the equatorial plane are
612 illustrated for E event and W event in the Figure (viewed from north of the equatorial plane).
613
614
615 Figure 2.
616 A progress of field line thinning in the growth phase is illustrated. The inflow flux ($F_{\perp}$) rotated
617 counterclockwise in times designated by red, green, and to blue arrows north of the
618 equatorial plane. South of the equatorial plane, rotation was in a clockwise direction. The
619 rotation of the inflow vectors produced the field-aligned component of the flux,
620 $\delta F_{//} = F_{\perp}(\omega \cdot \delta t)$ as depicted in the inset with one in the northern hemisphere shown. Note
621 that inflows are localized earthward of the outer field lines.
622
623
624 Figure 3.
625 Simulated pitch angle spectrogram of energy flux for drift Maxwell distributions of phase
626 space density. Energy flux was shown in contour plots with arbitrary amplitudes. To show
627 how the pitch angle spectrogram evolves, drift velocities in parallel and perpendicular
628 directions with respect to the background magnetic fields have changed. No drifts in both
629 perpendicular and parallel to the background field lines (A). Only parallel drifts increased;
630 $0.3V_{th}$ (B), $0.6V_{th}$ (C) and $1.0V_{th}$ (D). For (E) and (F), perpendicular drift increased to $0.3V_{th}$
631 and $0.5V_{th}$ while parallel drift remained at $1.0V_{th}$. V_{th} denotes thermal velocity. The vertical
632 axis is for pitch angles, while the horizontal axis is for particle energies normalized by the
633 thermal energy.

Figure 4.
(A) Multiple Pi2 event (1, 2, 3, and 4 labelled in the Figure) with positive bay observed at low latitude station (KUJ) at L=1.2 in the midnight sector (23:42 MLT at 15:00 UT). The figure, from 1430 UT to 1600 UT 31 August 1986, was reproduced from [Saka et al., 2002]. (B) Inclination angle of field lines in dipole coordinates along the satellite trajectories measured by AMPTE CCE spacecraft. Inclination angle (θ) was defined as $\theta = \mathrm{Tan}^{-1}\left(H/\sqrt{V^2+D^2}\right)$. H is positive northward parallel to the dipole axis, V is radial outward, and D is dipole east. Vertical arrows denote dipolarization onset corresponding to the multiple Pi2; 1, 2, 3, and 4 in panel A. (C) Difference of duskward flux (counts/sample) ($\mathbf{J}_-$) and dawnward flux ($\mathbf{J}_+$) for 63-85 keV ion channel measured by AMPTE CCE spacecraft. (D) Same as for (C) but for 125-210 keV ion channel.
Radial distance (R) in Re, MLaT in degrees, and MLT at 14:30 UT, 15:00 UT and 16:00 UT along satellite trajectory are shown in the bottom.

Figure 5.
A schematic illustration of particle measurement in X-Y plane of GSE coordinates; X is earthward, Y is duskward in ecliptic plane. For the time interval of multiple Pi2 event when the satellite was at 22 MLT, duskward flux represented by ($\mathbf{J}_-$) came from the earthward sector and dawnward flux ($\mathbf{J}_+$) from tailward sector. $\mathbf{J}_- > \mathbf{J}_+$ because of the pressure gradient positive earthward. Spatial gradient represented by solid line relaxed to dotted line. Radial separation, $X_1 - X_2$, is either 1000 km or 1800 km for 63-85 keV ions or 125-210 keV ions, respectively.

Figure 6.
A schematic illustration of the field line deformations in the meridian plane associated with the changing curvature radius of the field lines. The outer field lines marked by (1) changed to field lines (2) by increasing their curvature radius to R1 (red-dashed circle) in association with the relaxation of radial inhomogeneity, while the inner field lines marked by (3) moved

to field lines (4) of smaller curvature radius R2 (blue-dashed circle). This transition, (3) to (4), may be caused by the radial gradient of magnetic pressures becoming steeper in association with the inward compression of the field lines (see text). In the inset, flux tube deformations in the equatorial cross section is illustrated at onset locations (field lines 1 and 2). Divergence of perpendicular flows in dawn-dusk directions (solid arrows) produced dawn-dusk expansion of flux tube (2) coincide with the shrinkage of stretched flux tube (1). Flux tube deformation from 1 to 2 tended to preserve the total magnetic fluxes in the equatorial cross section.

Figure 7.

(A) Vertical component of $(rot\ \mathbf{J})_Z$ in the meridian chain along 300°E for the interval from 1000 UT to 1500 UT, reproduced from Saka and Hayashi (2017). Dipolarization onset was at 12:13 UT at this meridian. For the calculation of $(rot\ \mathbf{J})_Z$, vertical component data from RES (83.0°N, 299.7°E), CBB (76.6°N, 301.2°E), CONT (72.6°N, 298.3°E), YKC (68.9°N, 298.0°E), FSIM (67.2°N, 290.8°E), FSJ (61.9°N, 295.5°E), and VIC (54.1°N, 296.7°E) along the magnetic meridian 300°E were used (see text). Positive for the clockwise rotation (CW) of ionospheric currents and negative for the counterclockwise rotation (CCW) viewed from above the ionosphere. Amplitudes are color-coded. The scale is shown on the right. Demarcation lines separating CCW and CW in latitudes are marked by dashed line. The demarcation line moved to poleward after the onset. Note that negative $(rot\ \mathbf{J})_Z$ in poleward edge indicates smooth decrease of the Z amplitudes.

(B) Time progresses of the CW/CCW patterns are illustrated separately in five segments from 1 to 5 marked in Figure 7 (A). The figure demonstrates a progress of CW/CCW pair in time, CW in the poleward and CCW in the equatorward. This pair developed its size after onset showing poleward expansion. The meridional current associated with this pair of loop current, if closed in the equatorial plane via the field-aligned currents, comprised the Bostrom type current system.

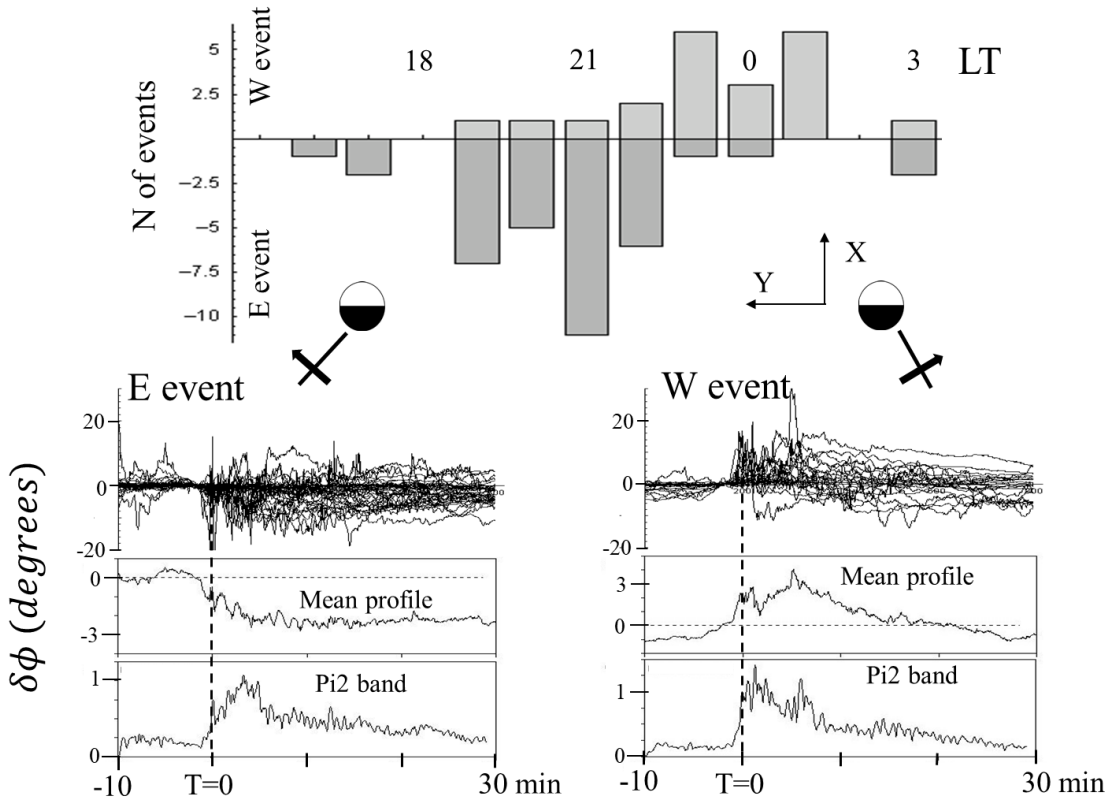
N of events
W event
E event
5
2.5
−2.5
−5
−7.5
−10
18
21
0
3
LT
X
Y
E event
W event
20
0
-20
Mean profile
Pi2 band
-10
T=0
30 min
$\delta\phi$ (degrees)

Figure 1

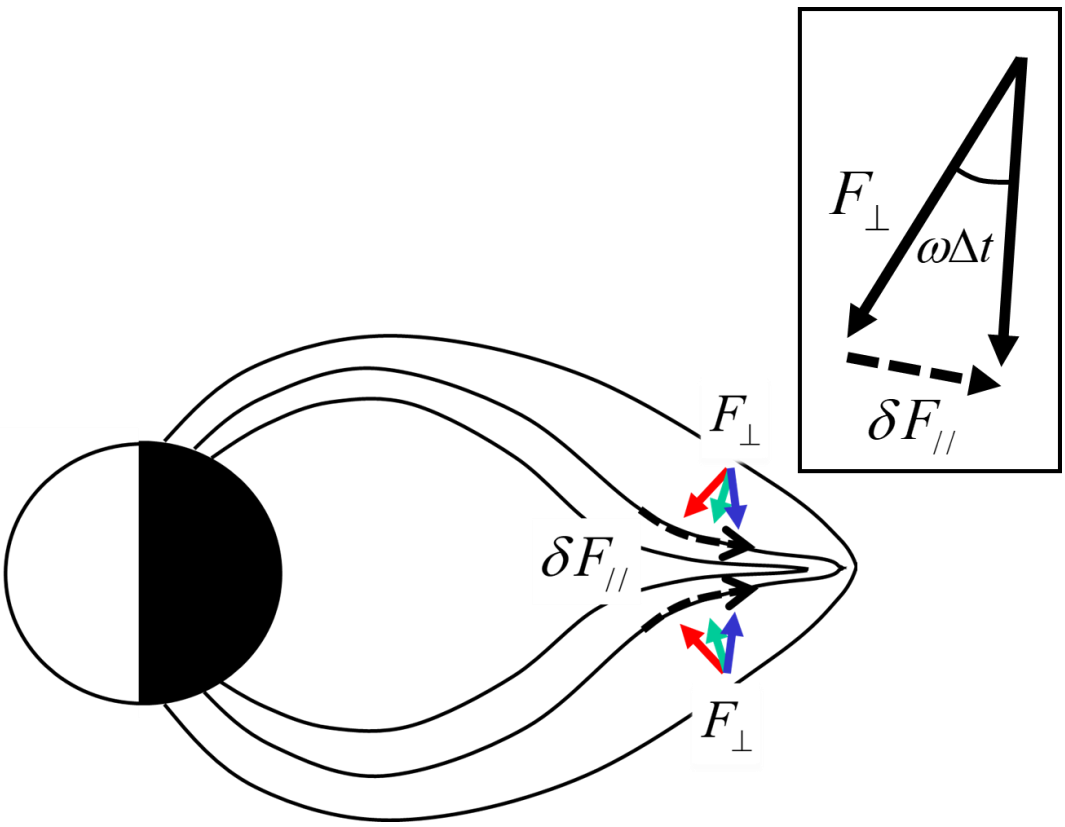

Figure 2

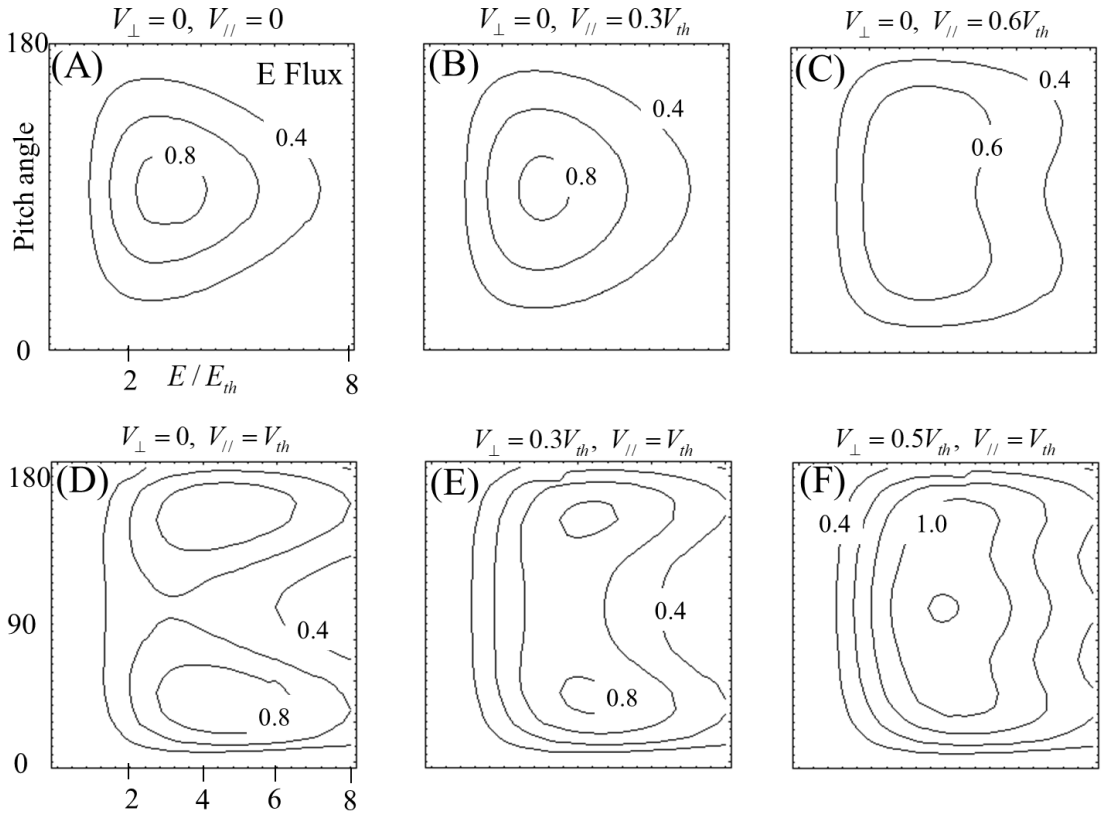
$V_\perp = 0,\ V_{//} = 0$
(A)
E Flux
180
0
Pitch angle
0.8
0.4
2
E / E_{th}
8
$V_\perp = 0,\ V_{//} = 0.3V_{th}$
(B)
0.4
0.8
$V_\perp = 0,\ V_{//} = 0.6V_{th}$
(C)
0.4
0.6
$V_\perp = 0,\ V_{//} = V_{th}$
(D)
180
90
0
0.4
0.8
2
4
6
8
$V_\perp = 0.3V_{th},\ V_{//} = V_{th}$
(E)
0.4
0.8
$V_\perp = 0.5V_{th},\ V_{//} = V_{th}$
(F)
0.4
1.0

Figure 3

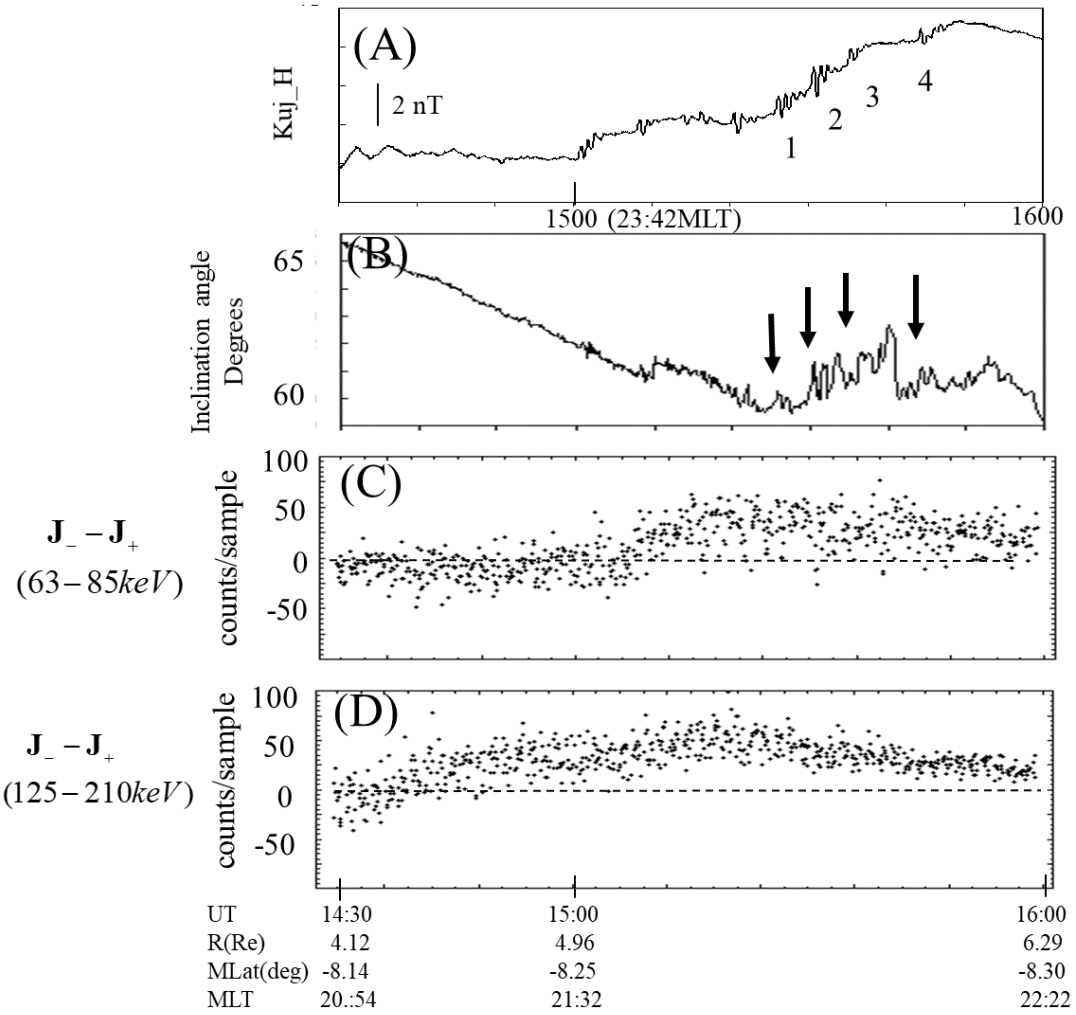
(A)
Kuj_H
2 nT
1
2
3
4
1500 (23:42MLT)
1600
(B)
Inclination angle
Degrees
65
60
(C)
$\mathbf{J}_- - \mathbf{J}_+$
$(63-85keV)$
counts/sample
100
50
0
-50
(D)
$\mathbf{J}_- - \mathbf{J}_+$
$(125-210keV)$
counts/sample
100
50
0
-50
UT 14:30 15:00 16:00
R(Re) 4.12 4.96 6.29
MLat(deg) -8.14 -8.25 -8.30
MLT 20.:54 21:32 22:22

Figure 4

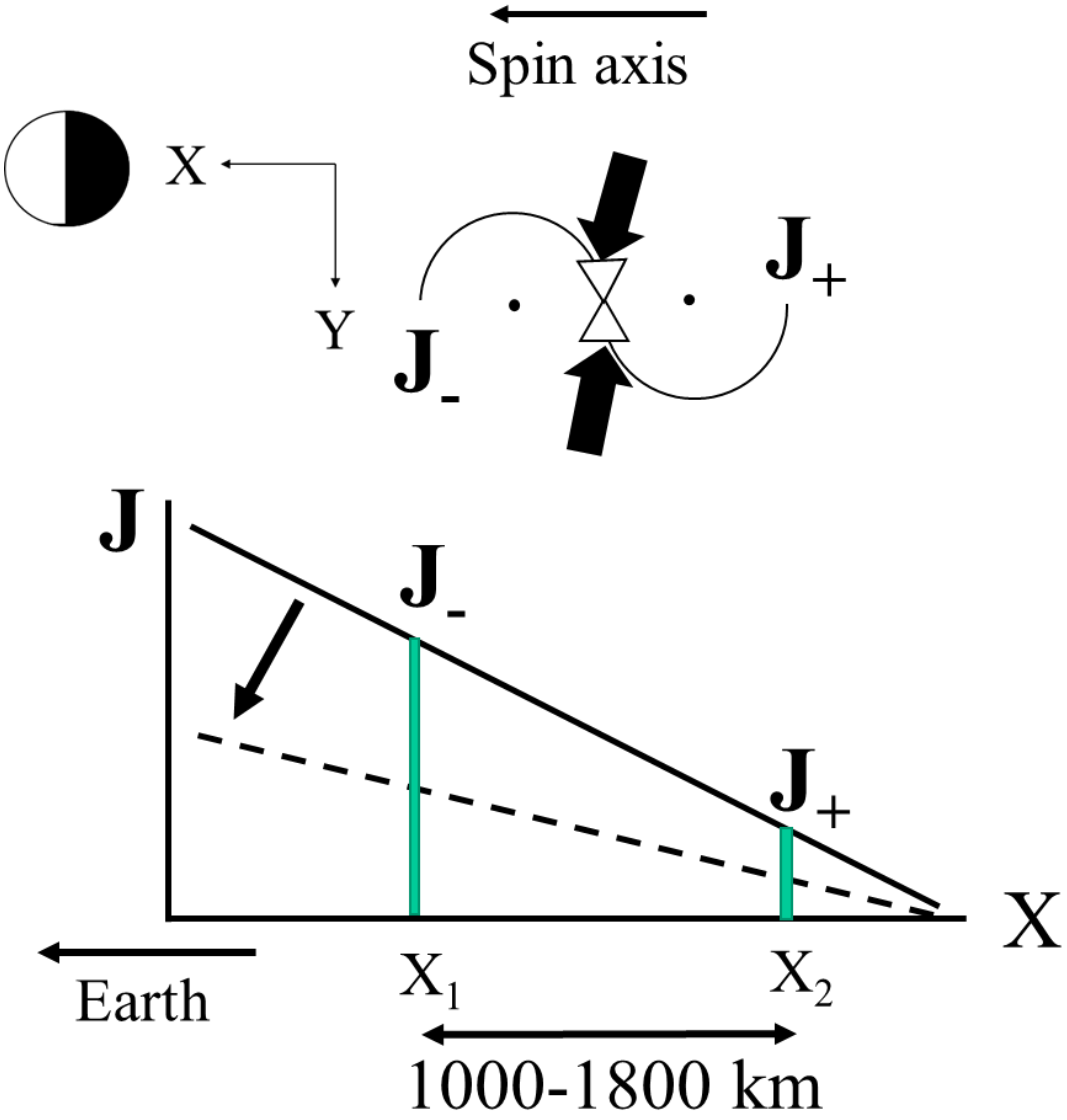

Figure 5

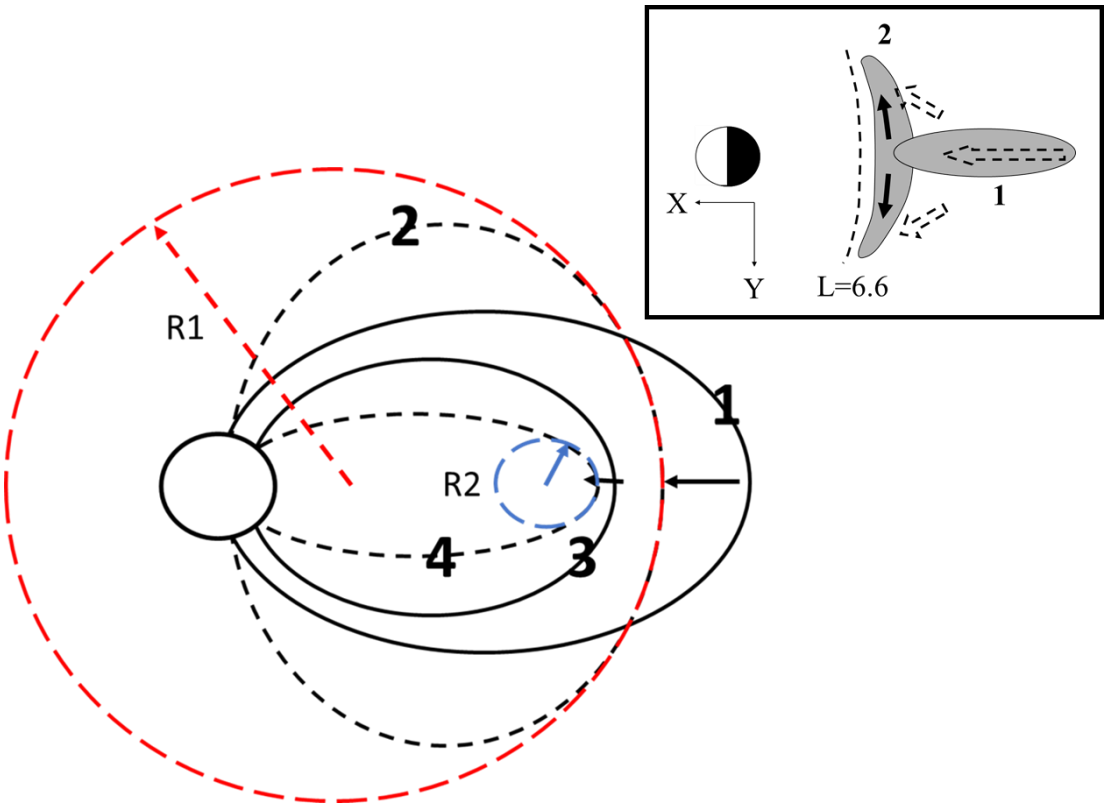

Figure 6

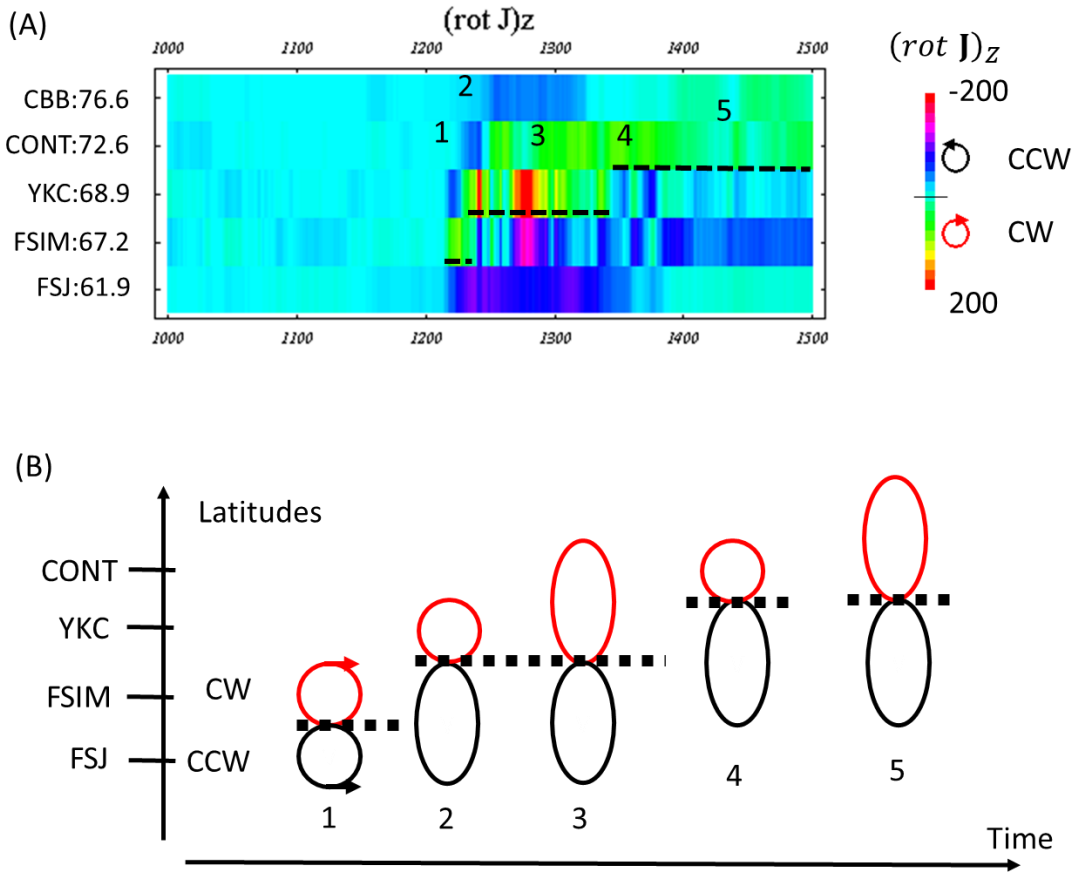
(A)
(rot J)z
1000
1100
1200
1300
1400
1500
CBB:76.6
CONT:72.6
YKC:68.9
FSIM:67.2
FSJ:61.9
1
2
3
4
5
$(rot\ \mathbf{J})_Z$
-200
CCW
CW
200
(B)
Latitudes
CONT
YKC
FSIM
FSJ
CW
CCW
1
2
3
4
5
Time

Figure 7